Robustness Analysis of Texture Features with Different Beamforming Techniques

Robustness Analysis of Texture Features with Different Beamforming Techniques

Silvia Seoni
PolitoBIOMed Lab, Biolab, Dept. of Electronics and Telecommunications
Politecnico di Torino
Torino, Italy
silvia.seoni@polito.it

Giulia Matrone
Dept. of Electrical, Computer and Biomedical Engineering
University of Pavia
Pavia, Italy
giulia.matrone@unipv.it

Kristen M. Meiburger
PolitoBIOMed Lab, Biolab, Dept. of Electronics and Telecommunications
Politecnico di Torino
Torino, Italy
kristen.meiburger@polito.it

***Abstract*—Texture features are often used on ultrasound images in various applications to give forth important clinical information. Recently, many beamforming techniques have been developed to provide better resolution and contrast in the final image. It is currently unknown, however, how these different techniques may also alter pixel intensity spatial distribution, known as texture. We provide here a robustness analysis of first and second order texture features using six beamforming techniques, on both phantom and *in vivo* musculoskeletal images. We show that second order texture features are more robust compared to first order features, especially when considering *in vivo* musculoskeletal images.**

Keywords—ultrasound beamforming, texture features, image processing, robustness

I. Introduction

Ultrasound images show a unique speckle pattern, which results from the interaction between tissue components and the ultrasonic wave [1]. The speckle pattern is also known as the ultrasound image texture. Texture features are commonly used on ultrasound images to provide important clinical information, such as tissue/organ functionality and health [2]. First-order texture features depend only on the global pixel distribution (i.e., the luminosity histogram), whereas second-order features depend on the spatial distribution of pixel intensities and their relationship between each other. Texture features have shown to help discriminate cancerous tissue in ultrasound images of the thyroid, ovaries, liver, prostate, and breast [2]. Studies have also shown how texture features are useful in other applications, such as musculoskeletal ultrasonography [3], [4].

Recently, numerous beamforming techniques have been developed that provide a better resolution and contrast than the traditional delay and sum (DAS) method [5]–[7]. It is currently unknown, however, how different beamforming techniques, while improving resolution and contrast, may also alter ultrasound image texture. In this work, we provide a robustness analysis of commonly used first-order and second-order texture features using different beamforming techniques.

II. Material and Methods

A. Acquisition and Formation of Ultrasound Images

The dataset is composed of one phantom image (model 040GSE, CIRS Inc, USA), shown in Fig. 1, and two *in vivo* transversal images of the vastus lateralis muscle of a healthy subject (Fig. 2). The images were acquired using a 192-element linear array probe (model LA533, Esaote s.p.a., Florence, Italy) at 5 MHz (for the phantom) or 7 MHz central frequency (*in vivo* images), connected to the ULA-OP open system [8]. A 64-element aperture was used in transmission and reception. The transmitted signal was a 2-cycle, Hanning-tapered sinusoidal burst at the central frequencies mentioned. During phantom and *in vivo* acquisitions, the transmit focal depth was set to 20 mm and 25 mm, respectively. In reception dynamic focusing was always applied, and 192 scan lines were acquired.

The acquired raw radiofrequency (RF) signals, sampled at 50 MHz, were used to reconstruct B-mode ultrasound images using six different beamforming methods, which are now briefly described. A more comprehensive overview can be found in [5], [9].

Briefly, the RF signals $\hat{s}_i(t)$, with i=1…N, received by the N elements in the transducer array active aperture, were first focused by applying a proper set of focusing delays (τ_i) and then summed up, which is known as Delay and Sum (DAS) beamforming:

$$y_{DAS}(t) = \sum_{i=1}^{N} \hat{s}_i(t-\tau_i) = \sum_{i=1}^{N} s_i \quad (1)$$

where y_{DAS} is the DAS-beamformed output signal.

The other five beamformers are based on the concept of backscattered- echo spatial coherence. Firstly, the Filtered Delay Multiply and Sum (FDMAS) algorithm [5] computes the beamformed signal y_{FDMAS} as:

$$y_{FDMAS}(t) = BPfilter\left\{\sum_{i=1}^{N-1}\sum_{j=i+1}^{N} sign(s_i(t)s_j(t)) \cdot \sqrt{|s_i(t)s_j(t)|}\right\} \quad (2)$$

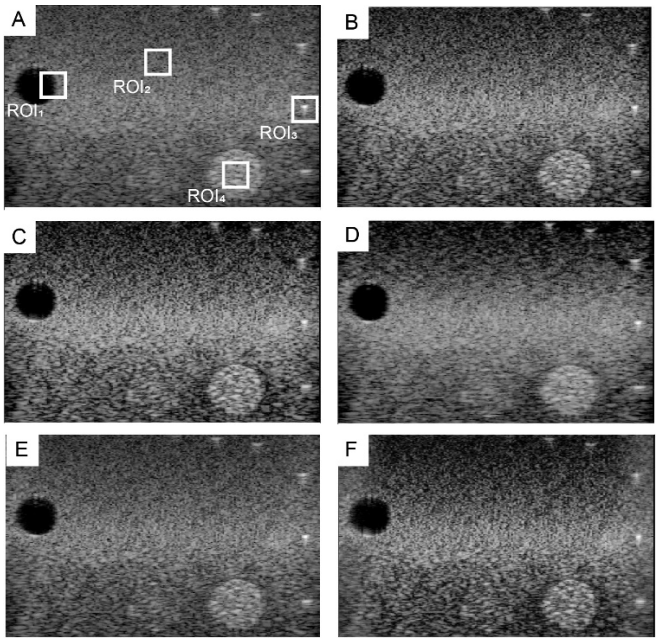

Fig. 1. Example of phantom image obtained with different beamforming techniques: A) DAS; B) FDMAS; C) CF; D) GCF; E) PCF; and F) SCF. Panel A) shows the manually-selected ROIs overlaid in white. The dynamic range value was automatically determinated for each image: DAS = 60 dB, FDMAS = 70 dB, CF = 85 dB, GCF = 70 dB , PCF = 70 dB and SCF = 85 dB.

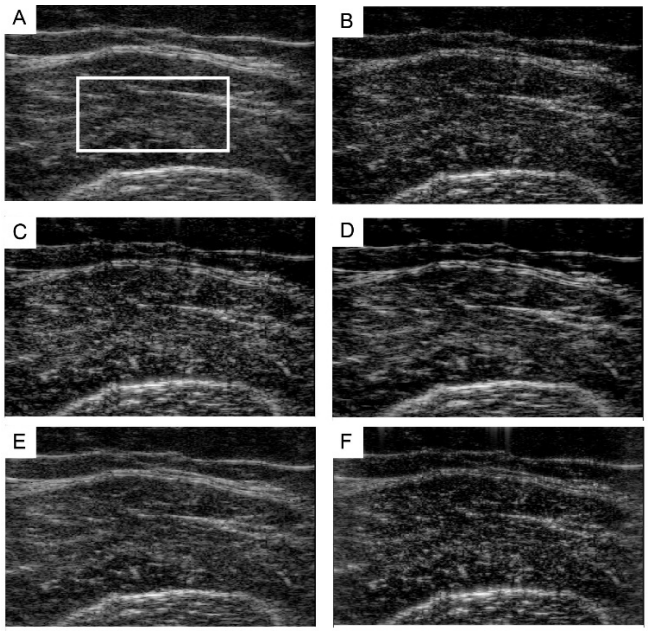

Fig. 2. Example of *in vivo* transversal images of the vastus lateralis muscle ($Vasto_1$) of a healthy subject obtained with different beamforming techniques: A) DAS; B) FDMAS; C) CF; D) GCF; E) PCF; and F) SCF. Panel A) shows the manually selected ROI. The dynamic range was automatically estimated for each image: DAS = 55 dB, FDMAS = 75 dB, CF = 85 dB, GCF = 75 dB, PCF = 65 dB and SCF = 85 dB.

where *BPfilter* represents a band-pass filter, which was set to pass the second harmonic component at twice the frequency of the transmitted signal.

The other implemented algorithms were the coherence factor (CF) [10], generalized CF (GCF) [6], phase and sign CF (PCF and SCF) [11]. These methods, differently from FDMAS, are based on the computation of a weighting matrix which is applied to the DAS-beamformed image in the following way:

$$y_{CF}(t) = y_{DAS}(t) \cdot CF(t) = y_{DAS}(t) \cdot \frac{\left|\sum_{i=1}^{N} s_i(t)\right|^2}{N\sum_{i=1}^{N} \left|s_i(t)\right|^2}, \quad (3)$$

$$y_{GCF}(t) = y_{DAS}(t) \cdot GCF(t) = y_{DAS}(t) \cdot \frac{\sum_{k=0}^{M_0} |S(k,t)|^2}{\sum_{k=0}^{N-1} |S(k,t)|^2} \quad (4)$$

$$y_{PCF}(t) = y_{DAS}(t) \cdot PCF(t) = y_{DAS}(t) \cdot \max\{0,\ 1 - \frac{\gamma}{\pi/\sqrt{3}}\sigma(\varphi_i(t))\}, \quad (5)$$

$$y_{SCF}(t) = y_{DAS}(t) \cdot SCF(t) = y_{DAS}(t) \cdot \left|1 - \sigma(b_i(t))\right|^p, \quad (6)$$

where k represents the spatial frequency index, $S(k)$ is the spectrum of $s_i(t)$, M_0 is a spatial frequency threshold, γ and p are two user-defined parameters that can be employed to tune the sensitivity of PCF and SCF, respectively, $\sigma(\varphi_i(t))$ is the standard deviation of the signal instantaneous phases $\varphi_i(t)$, and $b_i(t) = \text{sign}(s_i(t))$.

In this work, the parameter M_0 was set to 2, while γ and p were both set to 0.8.

The final image in dB scale was obtained by computing the beamformed signal envelopes through the Hilbert transform, then normalizing it to its maximum value and applying a logarithmic compression.

To obtain the final 8-bit pixel image, the dynamic range was automatically computed [12] and a calibration factor of 0.06 mm/pixel was used in both directions.

B. Texture Feature Extraction

We analysed texture features computed on six different ultrasound images obtained using the same raw RF signals and reconstructed using the previously described beamforming techniques. To do so, four Regions-of-Interest (ROI) of the same dimensions (45x50 pixels^2) were manually placed on the phantom image, to consider ROIs including both a hypoechoic and a uniform section (Fig. 1.A, ROI_1), a uniform speckle region (Fig. 1.A., ROI_2), a reflector (Fig. 1.A, ROI_3), and a uniform hyperechoic region (Fig. 1.A, ROI_4). In the two *in vivo* musculoskeletal images, a rectangular ROI (160x285 pixels^2) was placed in between the two aponeurosis (Fig. 2.A). The ROI for the first *in vivo* musculoskeletal image is abbreviated as $Vasto_1$, and the ROI for the second image as $Vasto_2$.

A total of 49 texture features, which are described in the following paragraphs, were computed in each ROI for each beamforming technique.

TABLE I. MATHEMATICAL DESCRIPTION OF FIRST-ORDER FEATURES

Feature	Description
Mean (m)	$m=\sum_{i=1}^{M}\sum_{i=1}^{N}\frac{I(i,j)}{M\times N}$
Variance (σ^2)	$\sigma^2=\frac{\sum_{i=1}^{M}\sum_{j=1}^{N}\{I(i,j)-m\}^2}{M\times N}$
Skewness (S_k)	$S_k=\frac{1}{M\times N}\frac{\sum_{i=1}^{M}\sum_{j=1}^{N}\{I(i,j)-m\}^3}{\sigma^3}$
Kurtosis (K_t)	$K_t=\frac{1}{M\times N}\frac{\sum_{i=1}^{M}\sum_{j=1}^{N}\{I(i,j)-m\}^4}{\sigma^4}$
Entropy (Ent_1)	$Ent_1=-\sum_{x=1}^{N_g}hist(x)*\log_2(hist(x))$

I(i,j) denotes the input region of interest (ROI). M is the number of columns of the ROI. N is the number of rows of the ROI. N_g is the number of gray levels of the image. *hist* is the normalized histogram counts.

1) First-Order Features

Based on the first-order statistics, five features were extracted from the ROIs: mean, variance, entropy, kurtosis, skewness. Table I presents the mathematical description of these features.

2) Haralick Features

The Haralick features are based on the grey-level co-occurrence matrix (GLCM) [13]. The GLCM measures the number of times a specific intensity pattern between adjacent pixels is repeated. GLCM was computed for four angles, i.e. 0°, 45°, 90°, 135°, and the mean over all four directions was calculated. The mathematical description of the Haralick texture features are listed in the Table II.

3) Galloway Features

The Galloway features are mathematical descriptors of the run length matrix (RLM) [14]. The RLM is a matrix, in which each element represents the number of pixels with run length *i* and intensity *j* in a given direction. We estimated the Galloway features at the same 4 angles (0°, 45°, 90° and 135°), and computed the mean over all four directions. Table III shows the mathematical description of Galloway features.

C. Robustness Analysis

To evaluate the robustness of the texture features, we first computed the mean and standard deviation of each feature among the 6 analyzed beamforming methods. Then, the Coefficient of Variation (CoV) was computed as the ratio of the standard deviation and the mean, to evaluate the variability of the texture feature values among beamforming techniques. The CoV was computed on the average values over the four directions for the Haralick and Galloway features. A cut-off value of 0.1 was used; hence, if the CoV was equal or less than 0.1, the beamforming methods showed similar texture parameter values which were therefore considered robust among beamforming techniques. On the other hand, a CoV higher than 0.1 represented more variation in the texture feature values, and the texture features were not considered robust among beamforming methods.

TABLE II. MATHEMATICAL DESCRIPTION OF HARALICK FEATURES

Feature	Description
Symmetry (I_{sym})	$I_{sym}=1-\sum_{i=0}^{N_g-1}\sum_{j=0}^{N_g-1}\lvert i-j\rvert P(i,j)$
Contrast (I_{con})	$I_{con}=\sum_{n=0}^{N_g-1}n^2\left\{\sum_{i=0}^{N_g-1}\sum_{j=0}^{N_g-1}P(i,j)\right\}$
Homogeneity (I_{hmg})	$I_{hmg}=\left\{\sum_{i=0}^{N_g-1}\sum_{j=0}^{N_g-1}\frac{1}{1+(i-j)^2}P(i,j)\right\}$
Entropy (I_{Entr})	$I_{Entr}=-\sum_{i=0}^{N_g-1}\sum_{j=0}^{N_g-1}P(i,j)\log P(i,j)$
Correlation (I_{cor})	$I_{cor}=\frac{\sum_{i=0}^{N_g-1}\sum_{j=0}^{N_g-1}(i-j)P(i,j)-\mu_x\mu_y}{\sigma_x\sigma_y}$
Energy (I_{enrg})	$I_{enrg}=\sum_{i=0}^{N_g-1}\sum_{j=0}^{N_g-1}(P(i,j))^2$

P(i,j) is equal to $\frac{C(i,j)}{\sum C(i,j)}$, where *C(i,j)* represents the gray level co-occurrence matrix. N_g is the number of gray levels. $\sigma_x,\sigma_y,\mu_x,\mu_y$ are the standard deviations and means of P_x, P_y, the marginal probability density functions.

III. RESULTS

Table IV shows the CoV values for the six different ROIs and the considered texture features. The values in bold are those that are above the considered threshold (i.e., 0.1). As can be seen, the first order mean and entropy features were robust between beamforming methods (CoV<0.1) for all four phantom image ROIs, whereas the other three first-order features (i.e., variance, skewness and kurtosis) showed more variation (CoV>0.1). Considering the musculoskeletal *in vivo* images, however, all first-order features showed a CoV>0.1. The second order Haralick and Galloway features showed similar robustness considering both phantom and clinical images. In particular, the features that were found to be robust and showed similar values among beamforming methods were the Haralick I_{con}, I_{Entr}, I_{cor}, I_{Ener}, and the Galloway SRE, GLNU, RLNU, and RP.

TABLE III. MATHEMATICAL DESCRIPTION OF GALLOWAY FEATURES

Feature	Description
Short run emphasis (SRE)	$SRE=\frac{\sum_{i=1}^{N_g}\sum_{j=1}^{N_r}\frac{RLM(i,j)}{j^2}}{\sum_{i=1}^{N_g}\sum_{j=1}^{N_r}RLM(i,j)}$
Long run emphasis (LRE)	$LRE=\frac{\sum_{i=1}^{N_g}\sum_{j=1}^{N_r}j^2RLM(i,j)}{\sum_{i=1}^{N_g}\sum_{j=1}^{N_r}RLM(i,j)}$
Gray-level nonuniformity (GLNU)	$GLNU=\frac{\sum_{i=1}^{N_g}\left(\sum_{j=1}^{N_r}RLM(i,j)\right)^2}{\sum_{i=1}^{N_g}\sum_{i=1}^{N_r}RLM(i,j)}$
Run length nonuniformity (RLNU)	$RLNU=\frac{\sum_{i=1}^{N_r}\left(\sum_{j=1}^{N_g}RLM(i,j)\right)^2}{\sum_{i=1}^{N_g}\sum_{i=1}^{N_r}RLM(i,j)}$
Run percentage (RP)	$RP=\frac{\sum_{i=1}^{N_g}\sum_{j=1}^{N_r}RLM(i,j)}{N_g N_r}$

RLM: run length matrix. N_g represents the number of gray levels in the image (i.e., the number of rows of the matrix R), N_r represents the number of runs (i.e., the number of columns of the R matrix).

TABLE IV. COEFFICIENT OF VARIATION (COV) RESULTS

	ROI_1	ROI_2	ROI_3	ROI_4	$Vasto_1$	$Vasto_2$
Mean	0.057	0.064	0.051	0.070	**0.189**	**0.189**
Variance	**0.339**	**0.364**	**0.149**	**0.168**	**0.144**	**0.143**
Entropy	0.000	0.000	0.000	0.083	**0.387**	**0.376**
Kurtosis	**0.815**	**1.749**	**0.385**	**0.367**	**0.334**	**0.351**
Skewness	**0.236**	**0.203**	**0.166**	0.064	**0.198**	**0.203**
I_{sym}	**0.218**	**0.118**	**0.321**	**0.101**	**0.179**	**0.179**
I_{con}	0.009	0.019	0.015	0.006	0.019	0.020
I_{hmg}	**0.233**	**0.155**	**0.506**	**0.196**	**0.234**	**0.233**
I_{Entr}	0.047	0.035	0.069	0.050	0.040	0.040
I_{cor}	0.070	0.064	0.101	0.028	0.060	0.060
I_{Ener}	0.028	0.022	0.043	0.052	0.030	0.029
SRE	0.025	0.016	0.042	0.014	0.023	0.024
LRE	**0.142**	0.081	0.180	0.250	**0.183**	**0.164**
GLNU	0.097	0.081	0.110	0.046	0.069	0.074
RLNU	0.079	0.057	0.147	0.039	0.083	0.084
RP	0.035	0.025	0.062	0.053	0.040	0.039

I_{sym}: Haralick symmetry; I_{con}: Haralick contrast; I_{hmg}: Haralick homogeneity; I_{Entr}: Haralick entropy; I_{cor}: Haralick correlation; I_{enrg}: Haralick energy; SRE: Galloway short-run emphasis; LRE: Galloway long run emphasis; GLNU: Galloway gray level non uniformity; RLNU: Galloway run length non uniformity; RP: Galloway run percentage.

IV. DISCUSSION

In this preliminary study, we have analyzed if texture features computed on images obtained using different beamforming techniques are similar between each other or not. Specific features showed more variability among beamforming techniques, as shown in Table IV, but this should not be assumed to necessarily be a negative aspect. Here we have studied if texture features are robust among beamforming techniques, without taking into consideration if certain features computed on images obtained with different beamforming methods are able to better discriminate healthy from diseased tissue. Further studies are needed to confront this specific important aspect.

There are some limitations to this study. Firstly, the 8-bit images used in this study were obtained by automatically determining the dynamic range. Considering the phantom image, the dynamic range values were the following: DAS = 60 dB, FDMAS = 70 dB, CF = 85 dB, GCF = 70 dB, PCF = 70 dB and SCF = 85 dB. Both the *in vivo* musculoskeletal images were obtained using the same dynamic range: DAS = 55 dB, FDMAS = 75 dB, CF = 85 dB, GCF = 75 dB, PCF = 65 dB and SCF = 85 dB. Varying the dynamic range will produce images that are visually different, mainly in terms of pixel intensity, but perhaps also in terms of speckle pattern, and this aspect was not considered in this study. The high CoV values, especially for the *in vivo* musculoskeletal first-order texture features, could be partially due to the different image dynamic ranges. Secondly, here we have provided a robustness analysis for first-order and commonly used second-order features, but there are numerous higher-order features (i.e., [15]) that have not been included here, which will be analyzed in future studies.

V. CONCLUSION

We have presented a robustness analysis of first-order and second-order texture features using six different beamforming algorithms. We demonstrated how second-order texture features typically show more similar values among beamforming techniques when compared to first-order features, especially when considering *in vivo* musculoskeletal ultrasound images.

REFERENCES

[1] T. Szabo, *Diagnostic ultrasound imaging : inside out*. Elsevier Academic, 2004.

[2] O. Faust *et al.*, "Comparative assessment of texture features for the identification of cancer in ultrasound images: a review," *Biocybern. Biomed. Eng.*, vol. 38, no. 2, 2018.

[3] F. Molinari, C. Caresio, and U. Acharya, "Advances in quantitative muscle ultrasonography using texture analysis of ultrasound images," *Ultrasound Med. Biol.*, vol. 41, no. 9, pp. 2520–2532, 2015.

[4] K. M. Meiburger *et al.*, "Quantitative analysis of patellar tendon abnormality in asymptomatic professional 'Pallapugno' players: A texture-based ultrasound approach," *Appl. Sci.*, vol. 8, no. 5, 2018.

[5] G. Matrone, A. S. Savoia, G. Caliano, and G. Magenes, "The Delay Multiply and Sum Beamforming Algorithm in Ultrasound B-Mode Medical Imaging," *IEEE Trans. Med. Imaging*, vol. 34, no. 4, pp. 940–949, Apr. 2015.

[6] P. C. Li and M. L. Li, "Adaptive imaging using the generalized coherence factor," *IEEE Trans. Ultrason. Ferroelectr. Freq. Control*, vol. 50, no. 2, pp. 128–141, Feb. 2003.

[7] J. F. Synnevåg, A. Austeng, and S. Holm, "Adaptive beamforming applied to medical ultrasound imaging," *IEEE Trans. Ultrason. Ferroelectr. Freq. Control*, vol. 54, no. 8, pp. 1606–1613, 2007.

[8] E. Boni *et al.*, "A reconfigurable and programmable FPGA-based system for nonstandard ultrasound methods," *IEEE Trans. Ultrason. Ferroelectr. Freq. Control*, vol. 59, no. 7, pp. 1378–1385, 2012.

[9] G. Matrone, A. Ramalli, J. D'Hooge, P. Tortoli, and G. Magenes, "A Comparison of Coherence-Based Beamforming Techniques in High-Frame-Rate Ultrasound Imaging with Multi-Line Transmission," *IEEE Trans. Ultrason. Ferroelectr. Freq. Control*, vol. 67, no. 2, pp. 329–340, 2020.

[10] K. W. Hollman, K. W. Rigby, and M. O'Donnell, "Coherence factor of speckle from a multi-row probe," in *IEEE Int. Ultrason. Symp. IUS*, 1999, vol. 2, pp. 1257–1260.

[11] J. Camacho, M. Parrilla, and C. Fritsch, "Phase coherence imaging," *IEEE Trans. Ultrason. Ferroelectr. Freq. Control*, vol. 56, no. 5, pp. 958–974, May 2009.

[12] K. M. Meiburger, S. Seoni, and G. Matrone, "Automatic Dynamic Range Estimation for Ultrasound Image Visualization and Processing," in *IEEE Int. Ultrason. Symp. IUS*, 2020.

[13] R. M. Haralick, K. Shanmugam, and I. Dinstein, "Textural Features for Image Classification," *IEEE Trans. Syst. Man. Cybern.*, vol. SMC-3, no. 6, pp. 610–621, Nov. 1973.

[14] M. Galloway, "Texture analysis using grey level run lengths," *Comp Graph. Image Process*, vol. 4, pp. 172–179, 1975.

[15] Y. Shao and M. Celenk, "Higher-order spectra (HOS) invariants for shape recognition," *Pattern Recognit.*, vol. 34, no. 11, pp. 2097–2113, Nov. 2001.